Insight into the Influence of ZnO Defectivity on the Catalytic Generation of Environmentally Persistent Free Radicals (EPFRs) in ZnO/SiO_2 Systems

Massimiliano D'Arienzo[*1], Silvia Mostoni[1], Roberta Crapanzano[2], Cinzia Cepek[3], Barbara Di Credico[1], Mauro Fasoli [2], Stefano Polizzi[4], Anna Vedda[2], Irene Villa[2], and Roberto Scotti[1]*

[1] INSTM, Department of Materials Science, University of Milano-Bicocca, Via R. Cozzi 55, I-20125 Milano, Italy

[2] Department of Materials Science, University of Milano-Bicocca, Via R. Cozzi 55, I-20125 Milano, Italy

[3] Istituto Officina dei Materiali-CNR Laboratorio TASC, Strada Statale 14, km 163.4, I-34012 Trieste, Italy

[4] Dipartimento di Scienze Molecolari e Nanosistemi, Universit, Ca' Foscari Venezia and Centro di Microscopia Elettronica "G. Stevanato", Via Torino 155/b, 30172 Venezia-Mestre, Italy

ABSTRACT

The present study aims at supplying a more in-depth picture of the Environmentally Persistent Free Radicals (EPFRs) generation from phenol (PhOH) on ZnO/SiO_2 systems, by exploring the properties of ZnO nanoparticles with different intrinsic defectivity grown on highly porous silica with spherical (ZnO/SiO_2_S) and worm-like morphology (ZnO/SiO_2_W).

In detail, besides an extensive structural, morphological, and surface investigation, the occurrence of inequivalent defect centers in the samples was tracked by photoluminescence (PL) experiments, which unveiled, for ZnO/SiO_2_W, intense blue emissions possibly involving radiative recombination from Zn_i excited levels to the valence band or to V_{Zn} levels.

Electron Spin Resonance (ESR) spectra, corroborated these results and revealed a remarkably different behaviour of the samples in the EPFRs formation model reaction. In fact, upon PhOH contact, the ESR spectrum of ZnO/SiO_2_S showed the exclusive presence of a weak isotropic signal ascribable to a $PhenO^{\bullet}$ EPFR. Instead, for ZnO/SiO_2_W, intense features associated to oxygen species in proximity of V_O^+, V_{Zn}^- and $(V_{Zn}^-)_2^-$ centers dominate the spectra, while a minor contribution of $PhenO^{\bullet}$ radical can be discovered only by signals simulation. These outcomes definitively envisage a role of the intrinsic defectivity of ZnO NPs on the final yield and stability of EPFRs generation, with V_O^+ and V_{Zn}^- defects possibly involved in dissociative adsorption or oxidation processes at the oxide surface.

Although this work focuses on ZnO, it is expected to foster a critical re-examination and integration of important results on other metal oxide/silica systems already reported in the literature, offering the chance to better evaluate the dependence EPFRs generation on the oxide defects chemistry.

INTRODUCTION

The thermally activated interaction of aromatic molecules with metal oxides (such as iron, copper, zinc, and nickel oxides) enclosed in airborne fine and ultrafine particulate matter (PM) have been shown to generate radical species which are stable enough to persist in the atmospheric environment for days [1-7]. These environmentally persistent free radicals (EPFRs) are thought to generate DNA damage and induce pulmonary dysfunction, resulting from the onset of oxidative stress initiated by the radicals originated after exposure to PM and smoking [2-7]. Further, EPFRs represent intermediates for the generation of polychlorinated dibenzo-*p*-dioxins and dibenzofurans (PCDD/Fs), polycyclic aromatic hydrocarbons (PAHs) and their derivatives [8-12].

The general mechanism proposed for EPFRs formation entails the chemisorption of substituted aromatic molecules such as phenols, chlorophenols, and/or chlorobenzenes on the surface of transition metal oxides, which, successively, induces an electron transfer from the organic adsorbate to the metal center [13-15]. This results in a surface-bound organic radical and in the partial reduction of the metal cationic species, detected by electron spin resonance (ESR) and X-ray photoelectron spectroscopy (XPS) in CuO/SiO_2 [6,7], TiO_2/SiO_2 [15] and Fe_2O_3/SiO_2 [16] model systems, which simulate the PM particles [17, 18]. Recently the importance of the morphological features (e.g., the particle size, the specific surface area, metal clustering and distribution) on the radical generation have been also highlighted, confirming that the study of the EPFRs formation mechanism is essential in order to understand their properties and fate in the environment [19, 20].

In this frame, several recent efforts have been devoted to investigate the pathway of EPFRs formation on ZnO, which is known to provide phenoxy radicals with extraordinary lifetimes of 73 days [21-23]. This uncommon stability and low reactivity have been associated by Patterson et al. [23] to a charge transfer from ZnO toward the chemisorbed adsorbate, in evident contradiction to the previously cited EPFRs formation mechanism, which would involve the formation of Zn(I) species. In particular, by combining UPS and EELS experimental results, they primarily evidenced that, upon phenol (PhOH) chemisorption, EPFR generation is more favorable on polar (000-1) Zn-

terminated surface rather than on apolar (1010) surface, regardless the adopted contact temperature [22]. Successively, besides demonstrating by vibrational spectroscopy the formation of nearly identical phenoxy radicals both at room temperature and at 250 °C, they suggested by DFT calculations that the generation of EPFRs on (000-1) ZnO surfaces involves a coordination of the radical species to three Zn adjacent cations, supporting a charge transfer from the oxide to the adsorbate [23].

Although the mechanism proposed in such studies takes into account some properties of ZnO, like crystal structure and exposed surfaces, it delivers an incomplete picture of the complexity of the system, since the peculiar intrinsic defectivity typically detectable in this material, i.e. lattice vacancies (V_{Zn},V_O), Zn or O on interstitial sites (Zn_i, O_i), is not considered [24].

These defects are widely studied in the literature [25, 26] and are often associated with emissions in the visible region (violet ~2.9 eV, blue ~2.6 eV, green ~2.2 eV and yellow ~2.1 eV), whose attribution is still controversial. Moreover, some of them give rise to ESR active species: zinc vacancies when a hole is involved as lattice defect (V_{Zn}^-); zinc interstitial defects Zn_i^+, usually thermally or light-generated; oxygen ions (O^- and O_2^-); oxygen vacancies with one electron (V_O^+), i.e. F^+ centres [27-29].

All these defective species play a key role in determining the applications of ZnO especially in the field of heterogeneous catalysis [30-32] and sensing [33]. This envisages their involvement also in other surface-mediated processes, like those resulting in the EPFRs formation.

In this scenario, the present study reports on the experimental assessment of the EPFRs generation from phenol on ZnO nanoparticles (NPs) with different intrinsic defectivity supported onto highly porous silica (ZnO/SiO_2). This catalytic system mimics the PM particles.

In detail, ZnO NPs were grown directly on SiO_2 NPs with spherical and worm-like morphology (i.e. ZnO/SiO_2_S and ZnO/SiO_2_W), by a modification of a previously developed and consolidated sol-gel route [34, 35], which allows a homogeneous distribution of ZnO on silica surface. Besides a careful structural and morphological characterization of the materials, an extensive spectroscopic

investigation carried out by XPS and photoluminescence (PL) revealed the occurrence of various inequivalent defect centers and allowed to observe their electronic transitions.

Accordingly, ESR investigation corroborated a different intrinsic defectivity in the samples and, in particular, the occurrence of O^- and V_{Zn} in ZnO/SiO_2_W. Interesting correlations have been outlined between the stability of these defects and their influence on the reactivity of ZnO/SiO_2 systems with PhOH in the model reaction exploited to promote the EPFRs generation.

EXPERIMENTAL

Synthesis of ZnO/SiO_2. ZnO/SiO_2 powders were synthetized by a two-step reaction, developed by modifying a previously reported procedure [34, 35]. The method is fast, almost green (just ethanol and water as solvents) and generally allows to control the ZnO loading and to get a homogeneous distribution of the oxide in the final matrix.

First, SiO_2 particles with spherical (SiO_2_S) and worm-like (SiO_2_W) shape, nanometric size and very large specific surface area, were prepared according to [36, 37] and utilized as suitable matrix to simulate the particulate matter (step I).

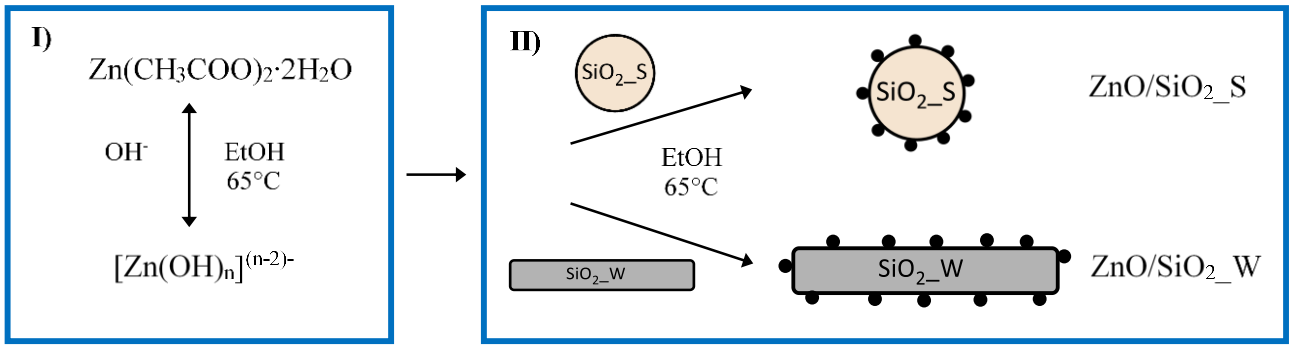

Scheme 1. Synthesis of ZnO/SiO_2 NPs [34, 35].

Successively, ZnO NPs were grown and anchored onto the surface of the two SiO_2 supports, exploiting a method reported in [34, 35] (step II). In detail, $Zn(CH_3COO)_2 \bullet 2H_2O$ (0.337 g) and NaOH (0.28 g) were dissolved in 50 mL of ethanol at 65°C; in the meantime, 1 g of SiO_2_S or SiO_2_W was dispersed in 20 mL of ethanol by sonication for 10 min (RT, pulses: 1 s; 20 kHz). Then the

SiO_2 dispersion was added to the former zincate solution and kept under stirring at 65 °C for 20 minutes. ZnO NPs formed by hydrolysis and condensation on the silica surface. After 20 min ZnO/SiO_2 particles were filtered, successively washed four times with ethanol and dried in air at room temperature (Scheme 1). The reactants amounts were chosen in order to obtain a nominally composition of the catalyst corresponding to 12 wt. % of ZnO on silica. The samples obtained from SiO_2_S and SiO_2_W were labelled as ZnO/SiO_2_S and ZnO/SiO_2_W, respectively.

Structural and morphological characterization.

The actual Zn loading was determined by Inductively Coupled Plasma Atomic Emission Spectrometry (ICP-AES), using a PerkinElmer OPTIMA7000 DV spectrophotometer.

Powder X-ray diffraction (PXRD) patterns were collected with a Brucker D8 Advance (Cu K_α radiation) in the range 20-70° 2θ (2θ step 0.025°, count time of 2 s per step).

Scanning electron microscopy (SEM) measurements were performed by a Vega TS5136 XM Tescan microscope in a high-vacuum configuration. The electron beam excitation was 30 kV at a beam current of 25 pA, and the working distance was 12 mm. In this configuration, the beam spot was 38 nm. Prior to SEM analysis, samples were gold sputtered.

High-resolution transmission electron microscopy (HRTEM) was performed using a Jeol 3010 apparatus operated at 300 kV with a high-resolution pole piece (0.17 nm point-to-point resolution) and equipped with a Gatan slow-scan 794 CCD camera. Samples were obtained by removing a film portion from the substrates in order to obtain a fine powder sample, then suspended in 2-propanol. A 5 μL drop of this suspension was deposited on a holey carbon film supported on a 3 mm copper grid for TEM investigation.

Nitrogen physisorption experiments were performed by using a Micromeritics ASAP2020 instrument, after evacuation of the samples at 180°C overnight. A liquid N_2 bath was used for measurements at 77 K. Specific surface area values (SSA_{BET}) were determined by the Brunauer-Emmett-Teller (BET) method.

Spectroscopic characterization.

XPS characterization. The surface chemical composition of the ZnO/SiO_2 powders was investigated by XPS. The measurements were performed on the as-prepared powders samples, fixing them on the sample holder using carbon tape. The XPS spectra were acquired in ultrahigh vacuum (base pressure: $\sim 5 \times 10^{-10}$ mbar) at room temperature in normal emission geometry using a conventional Mg X-ray source ($h\nu$ = 1253.6 eV) and a hemispherical electron energy analyzer (total energy resolution ~0.8 eV, standard deviation ±0.2 eV). Due to charging effects, all binding energies (BE) were calibrated by fixing the C 1*s* binding energy of atmospheric contamination at 284.8 eV. Survey scans were obtained in the 0–1100 eV range, while detailed scans were recorded in the BE regions corresponding to O 1s, C 1s, Si 2p, and Zn 2p levels. The O 1*s* and Zn $2p_{3/2}$ XPS spectra were reproduced by fitting the experimental data using a Shirley background and several Doniach-Sunjich components, corresponding to different oxidation states and chemical environments.

Photoluminescence. Steady state photoluminescence emission (PL) and photoluminescence excitation (PLE) spectra were measured by a continuous wave (CW) xenon lamp as excitation source coupled to a double monochromator (Jobin-Yvon Gemini 180 with 1200 grooves/mm gratings), and recorded through a nitrogen cooled, back illuminated, UV enhanced, CCD (Charge-Coupled Device) detector coupled to a monochromator (Jobin-Yvon Micro HR with a 150 grooves/mm grating). Time-resolved PL (TRPL) spectra have been collected in time correlated single photon counting mode using a FLS 980 spectrofluorometer by Edinburgh Photonics. TRPL measurements were carried out using a pulsed diode light emitting device (EPLED) emitting at 3.6 eV as excitation source with a pulse width of ~950 ps, and a pulsed diode laser (EPL) emitting at 3.1 eV with pulse width of ~75 ps. The signal was collected with a bandpass of 20 nm at different emission energies: at 2.1 eV and 2.3 eV for excitation at 3.6 eV and at 2.7 eV for excitation at 3.1 eV.

ESR investigation. ESR studies of ZnO/SiO_2 samples were carried out using a Bruker EMX spectrometer operating in X-Band, with a frequency modulation of 100 kHz, microwave power of 0.2 – 63 mW, magnetic field modulation of 2-5 Gauss and equipped with an Oxford cryostat operating in a range of temperatures between 4 and 298 K. Spectra on as-prepared samples were registered both at room temperature and at 130 K, mostly in static vacuum ($p < 10^{-1}$ mbar). Experiments aimed to detect EPFRs were performed in accordance with the Dellinger procedure [6].

In detail, a home-made contact system was utilized for the adsorption of molecular adsorbates onto the catalyst. The experimental setup consisted in a Schlenk-line connected both to vacuum and to inert gas (N_2) and provided with a pressure gauge. A tailor-made ESR reactor with the ZnO/SiO_2 samples, and a reservoir reactor containing the pollutant (PhOH) were connected to the line. Before any experiment, the system was evacuated down to $p < 10^{-1}$ mbar, in order to avoid any possible contamination.

For the contact, about 150 mg of ZnO/SiO_2 powders were charged in the ESR reactor. The system was then evacuated at $p < 10^{-1}$ mbar and simultaneously heated up to 503 K. ZnO/SiO_2 samples were successively contacted for 10 minutes at the same temperature with p = 20 mbar of PhOH. After exposure, the samples were again evacuated down to $p < 10^{-1}$ mbar for 1h at the dosing temperature to remove any residual physisorbed dosant.

The *g* values were calculated by standardization with a,a′ - diphenyl - b - picryl hydrazyl (DPPH). Care was taken to always keep the most sensitive part of the ESR cavity (1 cm length) filled. Spectra simulations and fits were performed using the SIM 32 program [38].

RESULTS AND DISCUSSION

Structural and morphological characterization of ZnO/SiO_2 samples.

ICP-AES analysis attested that the ZnO loading corresponds to 10.4±0.1 wt. % and 9.8±0.1 wt. % for ZnO/SiO_2_S and ZnO/SiO_2_W, respectively, i.e. values barely similar to the nominal ones (~ 12 wt. %), with a reaction yield of about 80% in both cases.

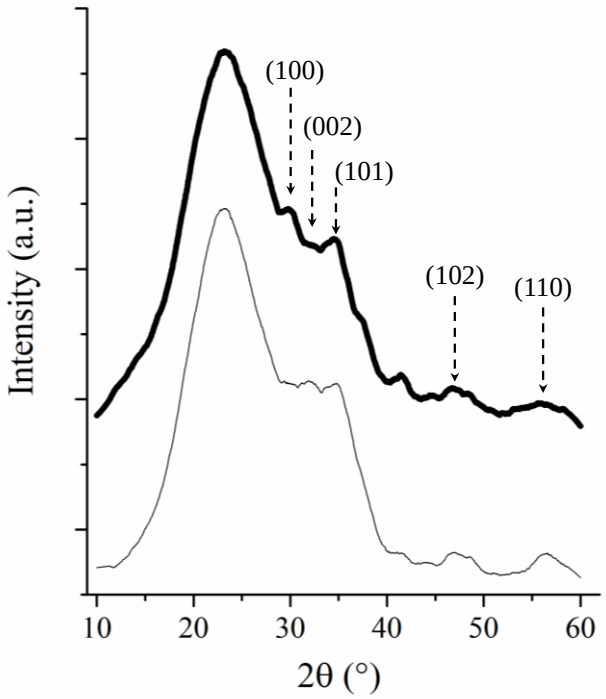

Figure 1. PXRD pattern of ZnO/SiO_2_S (black line) and ZnO/SiO_2_W (black bold line).

The structural features of ZnO/SiO_2 powders were investigated by PXRD diffraction. Figure 1 shows the pattern of the as-synthesized ZnO/SiO_2_S and ZnO/SiO_2_W samples. Besides the broad peak at ~22° connected to amorphous SiO_2 NPs, five main diffraction peaks can be identified and assigned to the hexagonal wurtzite ZnO crystal phase (JCPDS no.36-1451). A small increase in the relative intensity and sharpening of the (100) and (101) reflections is detectable going from ZnO/SiO_2_S to ZnO/SiO_2_W, suggesting a slightly higher crystallization degree and an increased average size for ZnO NPs anchored onto anisotropic silica surfaces.

The morphology of ZnO/SiO_2 particles was preliminarily inspected by SEM microscopy (Fig. 2). In detail, SEM micrographs showed that ZnO/SiO_2_S is constituted by quite uniform silica nanospheres with average diameter of ~ 80 nm (Fig. 2a), while for ZnO/SiO_2_W elongated nanoparticles with rod-like morphology and average length of ~ 400 nm have been observed (Fig. 2b).

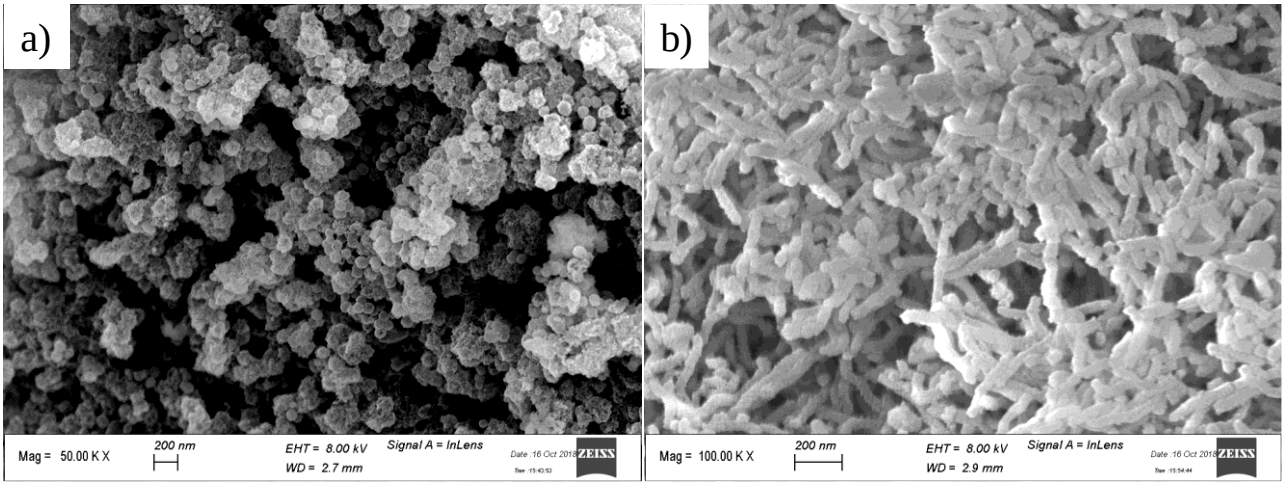

Figure 2. SEM micrographs of: a) ZnO/SiO_2_S; b) ZnO/SiO_2_W particles.

In order to gain deeper insight into the morphological features of ZnO/SiO_2 samples, TEM investigation was carried out (Fig. 3). The images of ZnO/SiO_2_S revealed that SiO_2 NPs actually are even smaller in size, with an average diameter of ~ 30 nm (Fig. 3a, b). In the case of ZnO/SiO_2_W, besides the evident worm-like morphology (Fig. 3d), the occurrence of an ordered mesoporous channel structure of few nanometers in diameter can be detected (Fig. 3e).

High resolution images (HRTEM) allowed to identify almost spherical or slightly elongated ZnO nanocrystals (average diameter/length ~ 5 nm), with well detectable crystallographic planes, homogeneously decorating the silica surface, whose crystallinity seem slightly more relevant in ZnO/SiO_2_W NPs (Fig. 3c and f), in accordance with PXRD indications.

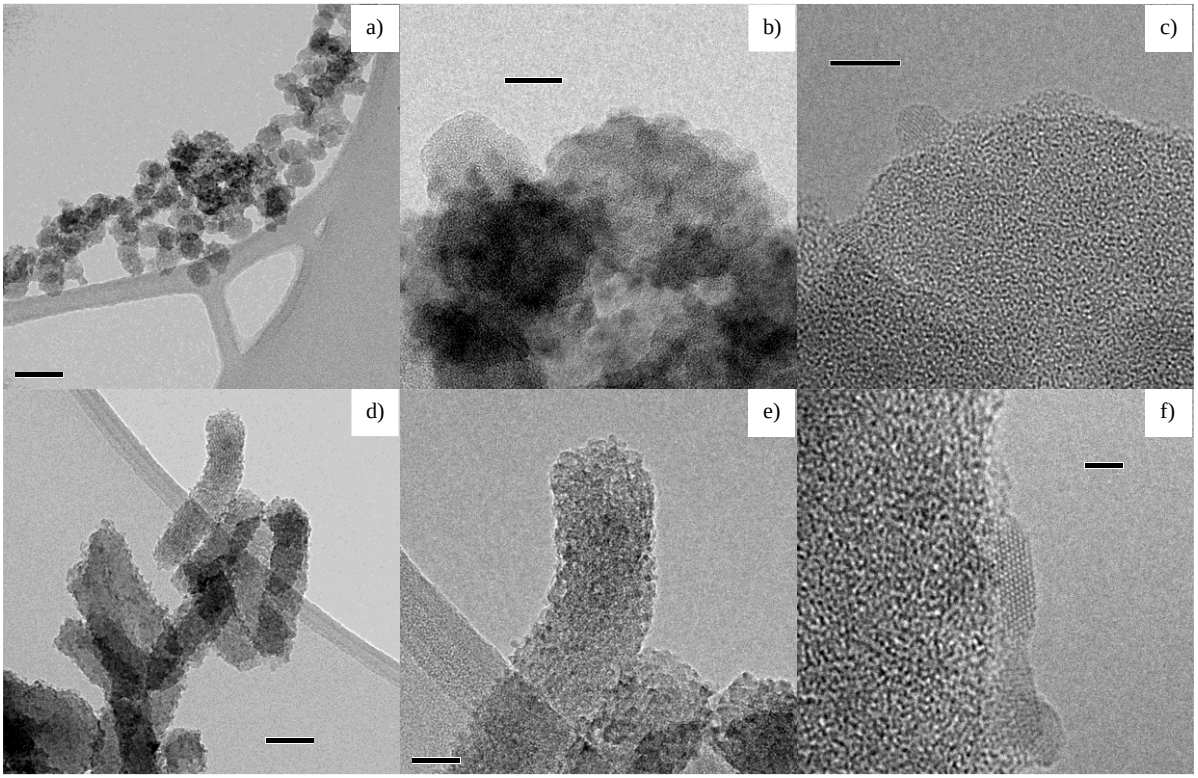

Figure 3. TEM and HRTEM images of: a)-c) ZnO/SiO_2_S and d)-f) ZnO/SiO_2_W. Insets in c) and f) highlight the crystalline nature of ZnO nanoparticles anchored on the surface of amorphous silica in ZnO/SiO_2_W.

Nitrogen physisorption experiments revealed a slightly different behavior of the samples (Fig. 4 and Table 1). ZnO/SiO_2_S shows a type II- IV combination of Brunauer isotherm (Fig. 4a) with a very narrow hysteresis loop. ZnO/SiO_2_W displays instead a type I - type IV combination of isotherms, typical of micro-mesoporous material, i.e. presenting both well-developed microporosity and some mesopores.

The modelling of the isotherm by nonlocal density functional theory methods (NLDFT) [39, 40] in order to obtain the pore size distribution (Fig. S1, Supporting Information), revealed that the mesopore size corresponds the silica intrinsic mesoporosity.

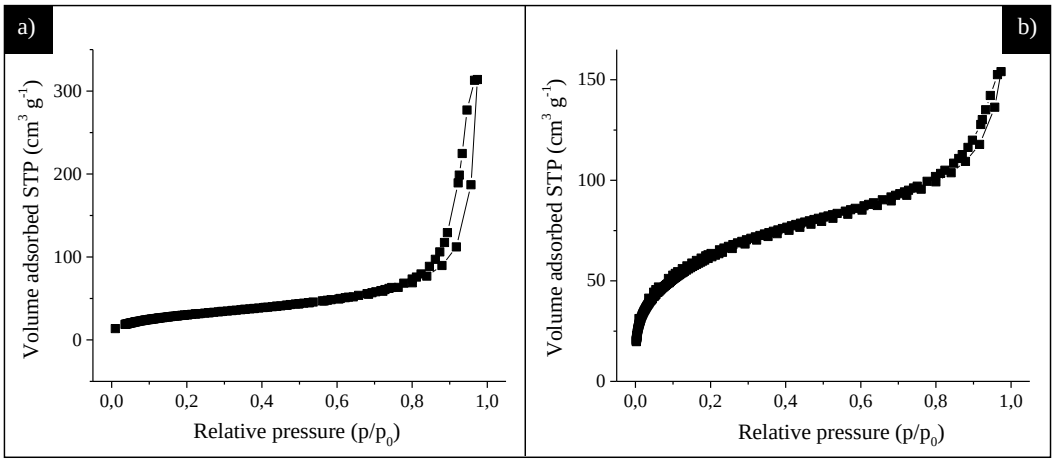

Figure 4. Adsorption/desorption isotherm at liquid nitrogen temperature for a) ZnO/SiO_2_S and b) ZnO/SiO_2_W sample.

Table 1 – SSA_{BET} and Desorption Cumulative Pore Volume (DCPV) values determined for ZnO/SiO_2_S and ZnO/SiO_2_W particles.

Sample	**SSA_{BET} (m^2/g)**	**DCPV (cm^3/g)**
ZnO/SiO_2_S	110.1±0.4	0.486
ZnO/SiO_2_W	216.8±1.3	0.238

These results indicate a relevant porosity for both the systems, even if the decoration with ZnO nanocrystals probably leads to the occlusion of the silica mesopores, thus reducing the whole pore volume and the total surface area in comparison to the pristine materials (see SSA_{BET} and DCPV values for SiO_2_S and SiO_2_W reported in Table S1, Supporting Information)

In summary, the morphological investigation unveiled the achievement of a homogeneous ZnO distribution onto the surface of amorphous silica NPs, without excessive clustering of the metal oxide in large aggregates.

Spectroscopic characterization of ZnO/SiO_2

XPS characterization. XPS analysis was carried out to further study the composition of the prepared ZnO/SiO_2 systems (Fig. 5 and 6). Fig 5 shows the typical XPS wide survey spectra of ZnO/SiO_2 samples and of the corresponding SiO_2 nanoparticles utilized as support. Zn, O and C peaks were detected. The presence of C in SiO_2 powders is related to the carbon adsorbed on the surface during the exposure of the sample to the ambient atmosphere while, in ZnO/SiO_2, it may be ascribed also to residual acetate species derived from the Zn precursor utilized for the materials synthesis. All binding energies were corrected for the charge shift using the C 1s peak of graphitic carbon (BE = 284.8 eV) as a reference.

Zn $2p_{3/2}$ XPS spectra of ZnO/SiO_2_S and ZnO/SiO_2_W are presented in Figure 6a. For both the samples, the Zn $2p_{3/2}$ spectra are found at ~1023.2 ± 0.2 eV, typical of Zn−O ionic binding [41]. However, in pure ZnO this level is usually detected at lower binding energies (BE ~ 1021 eV) [42]. The shift to higher BE suggests a change in the binding state of Zn ions, which can be induced by the formation of Zn−O−Si bonds at the interface between the ZnO and SiO_2 NPs in ZnO/SiO_2 samples. In detail, the higher Si electronegativity (1.9 eV) compared to that of Zn (1.65 eV), may activate a charge transfer from zinc to oxygen in ZnO/SiO_2 particles, which induces a decrease of the shielding effect of the valence electrons in Zn ions and, consequently, an increase of the BE of the core electrons of ZnO [41]. Moreover, as concerns on the position of Zn 2p3/2 peak, we cannot exclude the presence of different Zn-OH species at the surface [34].

O 1*s* XPS spectra of SiO_2_S, SiO_2_W, and ZnO/SiO_2 samples (Fig. 6b) display remarkable differences. The O 1*s* level in ZnO/SiO_2 is significantly broader than that observed for the pure silica nanoparticles, suggesting the occurrence of oxygen species in a different chemical environment. Indeed, spectral deconvolution resulted in two bands centered at 533.4 ± 0.2 eV and 531.8 ± 0.2 eV (Fig. 6b), which were assigned to oxygen atoms in silica and in the wurtzite ZnO crystalline network, respectively [41-43]. The presence of this low energy component, which appears more evident in ZnO/SiO_2_W, supports the crystalline nature of ZnO NPs and suggests a more

significant modification of the ZnO surface in this sample, due to the anchoring on anisotropic silica.

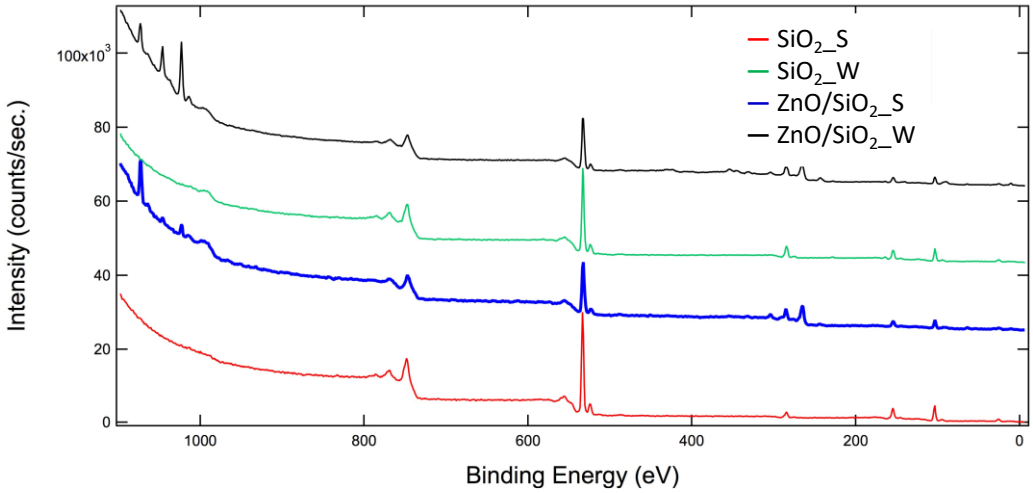

Figure 5. XPS wide survey spectra of SiO_2_S, SiO_2_W, ZnO/SiO_2_S and ZnO/SiO_2_W samples.

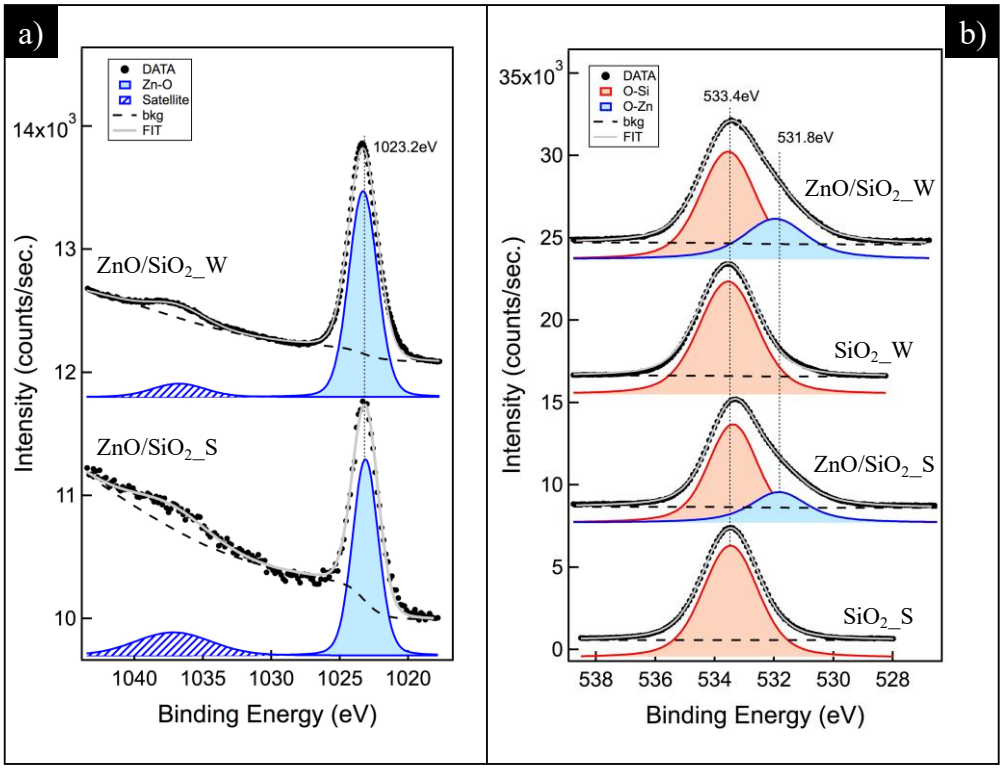

Figure 6. a) Zn 2*p3/2* and b) O 1*s* XPS spectra of SiO_2_S, SiO_2_W, ZnO/SiO_2_S and ZnO/SiO_2_W samples.

Photoluminescence measurements. Steady-state and time resolved PL measurements were carried out to study the optical properties of ZnO/SiO_2 systems (Fig. 7). Figs. 7a and 7b show, that exciting above the energy band gap of ZnO (Exc = 3.5 eV and 3.7 eV, respectively), PL spectra of ZnO/SiO_2 _S and ZnO/SiO_2 _W are centred at 2.2 eV and the excitonic peak, usually centred at 3.3 eV [43], is not observed. The detected emission can be attributed to the presence of defect levels in the band gap of ZnO that compete with the excitonic one and cause a green luminescence slightly shifted toward the yellow region. Exciting below the energy gap of ZnO (Exc = 3.1 eV), only a composite emission of ZnO/SiO_2 _W centred at 2.6 eV (Fig. 7b) is observed, revealing the occurrence of defect centres not present in ZnO/SiO_2 _S. A Gaussian deconvolution of the PL spectrum of ZnO/SiO_2 _W excited at 3.1 eV was performed (Fig. S2, SI). As a general approach for the fit procedure, we chose to involve the minimum number of Gaussian components required to obtain a satisfactory spectrum reconstruction. The numerical analysis was conducted by starting from the energy peak values reported in the literature. The slight discrepancy between our results and the literature ones can be accounted for the different morphology and the distorted crystal structure affecting mostly nanometric systems. The fit is in very good agreement with the experimental curve considering three bands whose parameters are reported in Table S2 of SI. The first component, centred at 2.26 eV, is probably the same one also excited at 3.5 eV and it has been extensively reported in the literature [25, 26, 44]. The others two bands, excitable only at 3.1 eV, are responsible for the emission in the blue region. The second component is peaked at 2.55 eV and dominates the spectrum. A similar band was already observed in ZnO. For example, it has been detected in ZnO thin films [45] and nanotubes [46]. The third one, centred at 2.82 eV, was added to get a fully satisfactory fit in the energy region above 2.9 eV. Despite the weaker intensity, its occurrence is commonly detected [6]. The reliability of the fit is therefore supported by previous literature investigations in which the bands involved were already detected. PLE spectra of the two systems corroborate PL results, confirming the presence of distinct defective species: ZnO/SiO_2 _S shows one PLE peak at 3.4 eV (emission recorded at 2.4 eV), while ZnO/SiO_2 _W shows two PLE peaks

at 3.1 eV and at 3.7 eV (emissions recorded at 2.7 eV and at 2 eV respectively). For comparison, Fig. 7c displays the absolute PL intensities of the various samples taken under the same experimental conditions. The emission at 2.2 eV of ZnO/SiO_2 _S is an order of magnitude more intense than in ZnO/SiO_2 _W, which displays instead a relevant blue emission. The weak emission of ZnO/SiO_2 _W at 2.2 eV could be related to either a lower concentration of the emitting defect centres responsible for the green luminescence or to the existence of an effective quenching channel. In the inset of Fig. 7c, the PL spectra of pristine SiO_2 _S and SiO_2 _W NPs are reported. Their intensity is negligible in comparison with the emission of the ZnO/SiO_2 samples, supporting the attribution of the optical properties of the systems completely to ZnO species anchored on the silica NPs. This is confirmed also by radioluminescence spectra collected on pristine silica nanopowders (not shown), which demonstrate that the composite emissions at ~ 2.4 eV detected in ZnO/SiO_2 samples are not connected to the silica substrate.

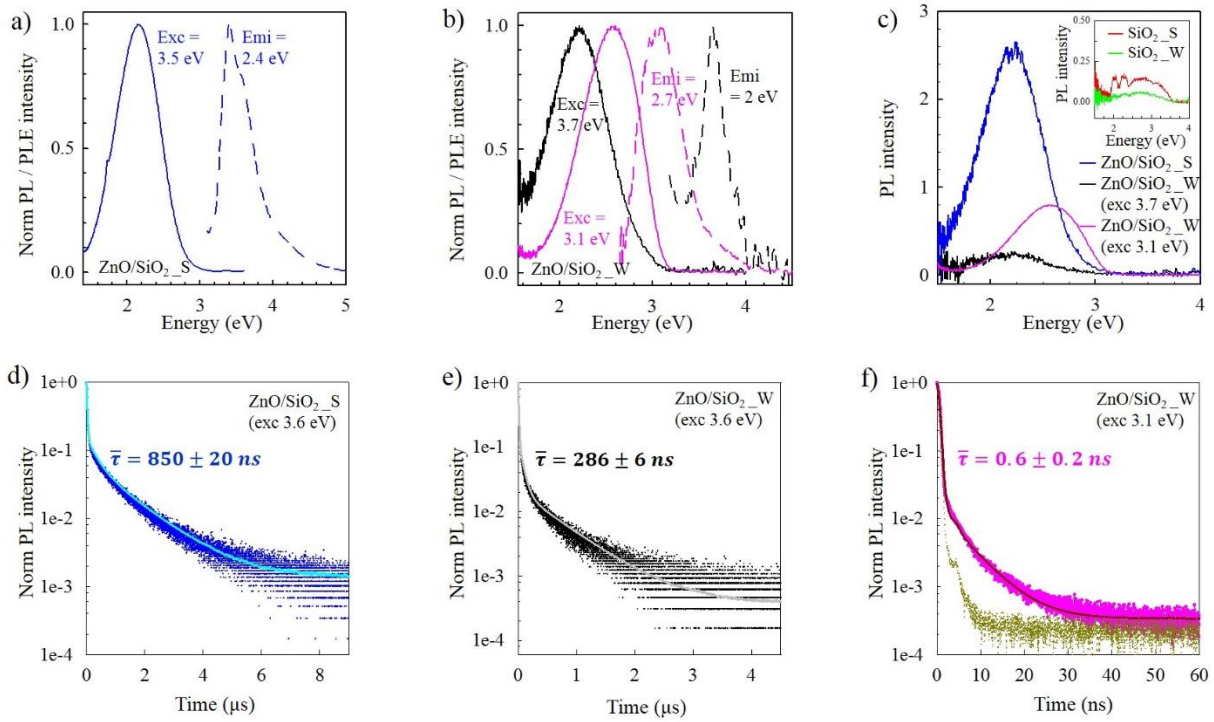

Figure 7. a) Normalized PL and PLE spectra of ZnO/SiO_2 _S. The PL spectrum (solid blue line) is recorded under CW excitation at 3.5 eV. The PLE spectrum (dashed blue line) is monitored at 2.4 eV. b) Normalized PL and PLE spectra of ZnO/SiO_2 _W. The PL spectra are recorded under CW

excitation at 3.7 eV (solid black line) and at 3.1 eV (solid pink line). The PLE spectra are monitored at 2 eV (dashed black line) and 2.7 eV (dashed pink line). c) PL spectra recorded under CW excitation of ZnO/SiO_2 _S at 3.5 eV (blue line), ZnO/SiO_2 _W at 3.7 eV (black line), and ZnO/SiO_2 _W at 3.1 eV (pink line). Inset: PL spectra of SiO_2 _S (red line) and SiO_2 _W (green line) recorded under CW excitation at 4.1 eV. d, e) PL time decays of ZnO/SiO_2 _S (dotted blue line) at 2.1 eV and of ZnO/SiO_2 _W (black dotted line) at 2.3 eV under pulsed excitation at 3.6 eV. f) PL time decay of ZnO/SiO_2 _W (pink dotted line) at 2.7 eV under pulsed excitation at 3.1 eV. The instrument response function is also shown (mustard dotted line). From d to f, the signal decays are fitted as a multi-exponential function (solid lines) and the average lifetime values are reported. The sets of all parameters used to model the PL decay are reported in Tables S3-S5 in SI.

To further investigate the defect-related emissions, TRPL measurements were performed. The signal decays of the green emission of both ZnO/SiO_2 _S and ZnO/SiO_2_W samples, recorded at 2.1 eV and 2.3 eV, respectively, can be fitted with a three-exponential function (Figs. 7d, e and Tables S3-S4 in SI). The average lifetime of ZnO/SiO_2 _W signal ($\overline{\tau}$ = 286 ± 6 ns) is shorter than the one of ZnO/SiO_2 _S ($\overline{\tau}$ = 850 ± 20 ns), supporting the occurrence of additional quenching centres in ZnO/SiO_2 _W. Fig. 7f reports instead the time decay of the blue emission of ZnO/SiO_2 _W recorded at 2.7 eV, which is fitted with a two-exponential function (Table S5 in SI). The different origin of this emission is enlightened by its average lifetime ($\overline{\tau}$ = 0.6 ± 0.2 ns), which is remarkably shorter than that at 2.2 eV in the same sample. For all the multiexponential PL decays, the complete data set of the obtained decay components with corresponding weight percentage are reported in Tables S3-S5 of SI.

According to the above experimental results, several considerations can be drawn. The green emission detected in both ZnO/SiO_2 _S and ZnO/SiO_2 _W is the most commonly observed in ZnO and also the most debated. It should be noted that in the literature [25, 26], the peak position of a band in this spectral region is reported ranging from 2.2 eV to 2.4 eV and different emission energies

sometimes are attributed to different defects. Several hypotheses have been proposed. The emission at 2.2 eV is usually attributed to transition from the singly ionized oxygen vacancy (V_o^+) to the valence band as verified by Camaranda et al. [47] monitoring the PL intensity during thermal annealing in O_2, and by Drouilly et al. [48] through ESR measurements. Li at al. [49] studied the green luminescence at 2.4 eV of ZnO nanowires with ultrafast PL techniques suggesting a recombination mechanism that involves electrons trapped in shallow levels with holes trapped in deep levels (~0.88 eV above the valence band). Moreover, green emission appears to be related also to surface defects, since it has been observed also that its intensity depends on the NP size [50], the substrate used for growth [51] and the terminating facets exposed [52]. In the present case, the green luminescence appears affected by the different structural, morphological and surface features of the ZnO/SiO_2 samples. In particular, the slightly higher crystallinity of ZnO NPs assessed by XRD and TEM as well as the presence of more significant modification of the ZnO envisaged by XPS in ZnO/SiO_2_W, seem to be connected toto the occurrence of a higher concentration of quenching channels in this sample as TRPL measurements suggest.

The intense blue emission observed exclusively in ZnO/SiO_2_W powders remarks its peculiar defectivity that affects the optical properties. This emission has been often associated to zinc interstitial defects (Zn_i) which are shallow donors that lie at ~0.3 eV [53] below the conduction band. Zeng at al. [54] observed that the blue PL can be excited by energies lower than the ZnO band gap, in agreement with our results. They proposed that the Zn_i levels, after the absorption of light, relax to the valence band emitting a photon with energy of ~2.9 eV. In any case, the emission in the blue region of ZnO/SiO_2 _W exhibits two sub-bands, centred at 2.82 eV and 2.55 eV, respectively (Fig. S2, SI). To explain these two components, Han et al. [55] proposed an emission mechanism involving also a zinc vacancy (V_{Zn}) which is a shallow acceptor that lies at ~0.3 eV [56] above the valance band. According to this hypothesis, the photogenerated electrons can decay from Zn_i levels to the valence band or to V_{Zn} levels emitting photons with energy of ~2.9 eV and ~2.6 eV, respectively. Thus,

ZnO/SiO_2 _W display defect centres absent in ZnO/SiO_2 _S and reasonably relatable to the presence of Zn_i and V_{Zn} species.

In conclusion, PL investigation highlights the occurrence of different optical properties for ZnO/SiO_2 systems, which foresee a role of defects in the reactivity of the materials.

ESR investigation

Several previous ESR studies in the literature reported thatthe adsorption of aromatic systems (i.e. chlorine- and hydroxy-substituted benzenes) on ZnO/SiO_2 surface leads to the generation of a surface-bound EPFR, similarly to the case of other transition metal oxides. In particular, Lomnicki et al. [21] argued that the half-lives of EPFRs formed on ZnO domains were the longest observed among the metal oxides studied and ranged from 3 to 73 days. Such remarkable radical stability was related to the low reducibility of Zn (II), thus corroborating the idea that the persistency of the EPFRs is rather dependent on their interaction with the metal oxide surface and not to their reactivity toward molecular oxygen [22]. More recently, other studies associated instead this uncommon behavior to a charge transfer from ZnO toward the chemisorbed adsorbate, which would involve the improbable formation Zn (I) species [23]. Nevertheless, the authors reasonably acknowledged that further comprehensive investigations are mandatory to fully elucidate the mechanism governing the generation and the stability of EPFRs on ZnO/silica [23].

Bearing in mind these concerns, here the PhOH interaction with ZnO/SiO_2 has been studied by ESR tracking also the peculiar intrinsic defects typically detectable in ZnO, as lattice defect (V_{Zn}), zinc interstitial (Zn_i), oxygen ions (O^- and O_2^-) and oxygen vacancies (V_O^+), which severely affect its surface reactivity and plausibly the EPFRs formation.

As a first step, pristine ZnO/SiO_2 samples were investigated. In detail, no spectral features have been detected for ZnO/SiO_2_S before the interaction with PhOH. ZnO/SiO_2_W displays instead a complex spectrum constituted by two groups of resonance lines, assigned to different defect centres (Fig. 8a).

At higher field, a weak and broad signal with g ~ 1.96, whose assignment is still under debate in the literature [24, 57, 58], can be observed. It is generally associated to singly ionized oxygen vacancy defects (V_O^+) or shallow donor centers, such as ionized impurity atoms in the crystal lattice of ZnO [57, 58]. Conversely, other reports infer that this ESR signal may be due to one electron being weakly bound to ionized impurities, e.g. Zn_i centers [59]. Thus, UV-irradiation is expected to excite them giving rise to paramagnetic species [60].

In the present case, UV-photoexcitation of ZnO/SiO_2_W sample at 130 K resulted in a partial increase of the very weak feature at g ~ 1.96 (not shown), suggesting that the signal is not related to oxygen vacancies, while it belongs to electrons from a shallow donor level located in impurity atoms [60].

The lower field overlapped signals g = 1.99-2.02 observed for ZnO/SiO_2_W have been widely reported in the literature for ZnO systems [61-67]. However, their assignment is still discussed. ESR investigations on bare ZnO performed under UV photoexcitation have attributed these spectral features to singly ionized Zn vacancies (V_{Zn}^-), while other studies ascribed them to V_O^+ centers. Recently, Erdem et al. [61-66] have proposed a *core-shell* model to describe the paramagnetic centers in ZnO nanoparticles. In their model, the ESR signal at g ~ 1.96 belongs to V_{Zn}^- species in the bulk (*core*), whereas those near g ~ 2.00 arise from different surface oxygen vacancy defects (*shell*).

Thus, in order to provide a fair attribution and to discriminate the overlapping signals at g = 1.99-2.02 occurring in ZnO/SiO_2_W, their saturation behavior as a function of the microwaves power have been studied (Fig. 8b). Increasing the power from 0.2 mW to 63.5 mW, the spectral feature at g ~ 2.01 (labelled with ◇) increases in intensity in the whole power range and does not saturate even at the maximum microwave power utilized. Instead, the signals at g ~ 2.02 and g ~ 2.00 (indicated with ✳) reach a maximum at 6.3 mW, indicating that signal saturation occurs in proximity of this power value (Fig. 8b).

These trends clearly prove the presence of different paramagnetic species, whose *g* values and relative contribution to the spectrum (calculated as % of the total intensity of overlapping signals at *g* = 1.99-2.02) were calculated by signal simulation.

Three different components have been identified (Table 2 and Fig. 8a): two overlapping orthorhombic signals (species I and II) and one almost isotropic line (species III).

According to previous studies [62, 63, 66, 67], they have been attributed to paramagnetic defects located in proximity to the surface of the ZnO nanoparticles: species I, with orthorhombic symmetry, to O_2^- centers associated to the presence of oxygen vacancies; species II, with roughly orthorhombic symmetry, to two mutually close zinc vacancies with one hole, i.e. $(V_{Zn}^-)_2^-$; species III, almost isotropic, to O^- species connected to the oxygen ions that surrounds V_{Zn}^- defects.

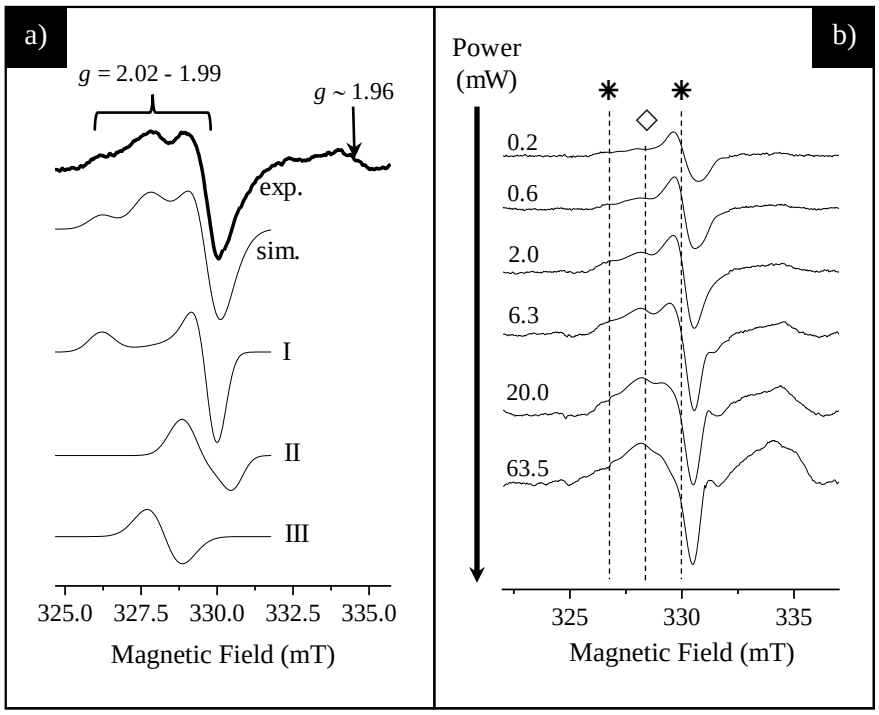

Figure 8. a) Experimental (exp.) and simulated (sim.) ESR spectrum at 300 K of ZnO/SiO_2_W powders. Deconvolution of signals of into species I-III is also reported. b) Spectra of ZnO/SiO_2_W recorded at different mW power at 300 K. The signal at *g* ~ 2.01 is labelled with ◇, while those at *g* ~ 2.02 and *g* ~ 2.00 with ✳. Dashed lines are guides to discriminate the trend of these different paramagnetic species.

The exposure of ZnO/SiO_2 systems to PhOH vapors allowed to emphasize even more their different defective structure and its influence on the surface reactivity of the materials (Fig. 9).

In detail, the ESR spectrum of ZnO/SiO_2_S recorded after PhOH exposure reveals the exclusive presence of a new weak isotropic signal at g = 2.0036 with linewidth of 8.3 G (Fig. 9a), which is highly stable and undergoes a noticeable decay only after 24 hours in air. This behaviour is typical of an EPFR [1-7] and, based on the g value, the resonance occurring at g = 2.0036 was assigned to PhenO$^{\bullet}$ radicals.

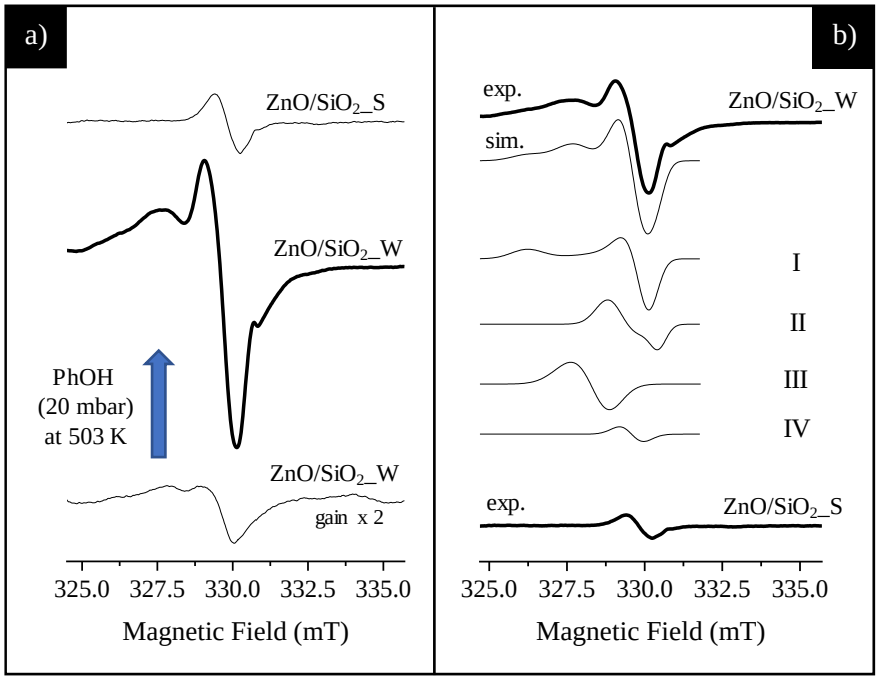

Figure 9. a) ESR spectra at 300 K of: ZnO/SiO_2_W powders before and after exposure to PhOH vapors at 503 K; ZnO/SiO_2_S after PhOH contact. b) Experimental (exp.) and simulated (sim.) spectra at 300 K of ZnO/SiO_2_W particles recorded after PhOH exposure. Deconvolution of signals of into species I-IV is reported. ESR spectrum of ZnO/SiO_2_S is also included for comparison.

After PhOH contact, ZnO/SiO_2_W displays a complex spectrum due to different overlapped resonance lines. The signal intensities are higher and linewidths larger than those of the ZnO/SiO_2_S powders. Besides, a rapid decay of the spectral features occurs upon air exposure. ZnO/SiO_2_W spectrum was simulated and fitted with four different lines (Figure 9b) whose values

are reported in Table 2. These characteristics and the simulation results indicated that the spectral features can be associated unambiguously to species I-III already observed in pristine ZnO/SiO_2_W and probably generated from the surface interaction between PhOH and ZnO. However, the fitting of the spectrum suggests the presence of a fourth isotropic center (species IV in Fig 9b) contributing to the spectrum at g = 2.0040 and with linewidth 8 G, attributable to the PhenO$^{\bullet}$ radical [20, 21].

The intensity of this signal is much lower than that detected for the same radical in ZnO/SiO_2_S (Table 2).

Table 2. g tensor values of the paramagnetic defects detected before and after PhOH contact for ZnO/SiO_2_W sample, determined by simulation of the ESR features. The relative contribution of the species (calculated as % of the total intensity of overlapping signals at g = 1.99-2.02) is also reported. The g-value of the EPFR (species IV) arising upon PhOH contact in ZnO/SiO_2_S is reported for comparison.

Species		**Pristine**		**After PhOH exposure**			
		ZnO/SiO_2_W		ZnO/SiO_2_S		ZnO/SiO_2_W	
		Contribution (%)	g value	Contribution (%)	g value	Contribution (%)	g value
I	O_2^- (V_O^+)	46.0 %	g_{zz} = 2.0243, g_{yy} = 2.0036, g_{xx}= 2.0010	/	/	47.0 %	g_{zz} = 2.0249, g_{yy} = 2.0036, g_{xx}= 2.0010
II	$(V_{Zn}^-)_2^-$	36.5 %	g_{zz} = 2.0077, g_{yy} = 2.0043, g_{xx}= 1.9980	/	/	23.6 %	g_{zz} = 2.0084, g_{yy} = 2.0049, g_{xx}= 1.9992
III	O^- (V_{Zn}^-)	17.5 %	$g_{\perp}$ = 2.0124, $g_{\parallel}$ = 2.0114	/	/	22.4 %	$g_{\perp}$ = 2.0129, $g_{\parallel}$ = 2.0119
IV	EPFR PhenO$^{\bullet}$	/	/	100%	g_{iso} = 2.0036	7.0 %	g_{iso} = 2.0040

The above outcomes support the PL results and substantiate the existence of various inequivalent defect centers in ZnO/SiO_2 systems. In particular, the peculiar paramagnetic defectivity of ZnO/SiO_2 _W enlightened by ESR spectra (i.e. oxygenated species in proximity of V_O^+, V_{Zn}^- , $(V_{Zn}^-)_2^-$ and Zn_i centers) appears connected to the intense blue emissions observed at ~ 2.9 eV and

~2.6 eV exclusively in this sample, which accordingly rely on photogenerated electrons that can decay from Zn_i levels to the valence band or to V_{Zn} levels emitting photons.

Further, the occurrence of these specific defects remarkably affects the final yield of EPFRs generation. In fact, V_O^+ and V_{Zn}^- defects in ZnO/SiO_2_W may promote a dissociative adsorption process on the substrate [68] leading, upon PhOH absorption, to ESR silent adduct or to its fast oxidation toward quinonic products. From the ESR spectra, it is also evident that the interaction of PhOH in mild vacuum conditions ($p < 10^{-1}$ mbar) creates further vacancy sites on the catalyst surface which can be filled then by the residual O_2 present in the stream forming new O_2^- and O^- centers. These species may act as oxidative sites for the organic molecule (i.e. Mars van Krevelen mechanism [69]), thus hampering the formation and stabilization of EPFR in ZnO/SiO_2_W.

With regard to the present study, the defectivity of ZnO NPs arising from the different structural, morphological and surface features of the ZnO/SiO_2 samples, has been considered as the trigger of their surface reactivity in the formation of EPFR. However, it must be observed that the silica NPs utilized as substrate for growing homogeneous ZnO NPs and mimicking the PM particles might play also a key role.

As extensively reported in the literature [70-72], several dangling type defects, e.g. non-bonding oxygen-hole centers (NBOHCs), peroxy radical centers (POR) and the so-called E' centers, can be detected in mechanically ground silica glass or in high surface area silica.

Although PL and EPR survey on both pristine and ZnO-modified SiO_2 NPs did not give any clear evidence about the presence of defect sites associated to the silica substrate, their possible occurrence in ZnO/SiO_2 systems cannot be excluded and surely represents a point that could be decisive for their interfacial reactivity. In fact, these species often behave as catalytically active sites, contributing to reactant adsorption and, in some cases, assisting reactants activation [73]. Thus, in the present case, they may be used to invoke a synergism between ZnO and silica in a catalytic sense, helping to explain the negligible formation and stabilization of EPFR in ZnO/SiO_2_W.

Nonetheless, the here presented evaluation clearly demonstrates that a fair assessment of the generation of EPFRs in metal oxide-based systems needs to primarily identify the nature of defects in the oxides, which can significantly impact on the yield and stabilization of these radical species.

CONCLUSIONS

The present study reports a comprehensive comparison between the properties and the reactivity in the EPFRs generation of ZnO/SiO_2 systems constituted of ZnO NPs homogeneously decorating mesoporous SiO_2 NPs with spherical and worm-like morphology.

The structural and morphological investigations, beside evidencing the occurrence of ZnO spherical NPs anchored to the silica surface, enlightened an enhanced crystallinity of the oxide when anisotropic silica particles were used as support. Added to these observations, XPS analysis emphasized the formation of Zn−O−Si bonds in both the systems, with a more significant modification of the ZnO surface in ZnO/SiO_2_W sample. These peculiar morphological and surface properties result in the occurrence of inequivalent defect centers in ZnO/SiO_2 systems. In particular, PL experiments evidenced that ZnO/SiO_2 _W displays intense blue emissions which are detectable only in this sample and can be ascribed to photogenerated electrons decaying radiatively from Zn_i levels to the valence band or to V_{Zn} levels. Accordingly, ESR spectra of ZnO/SiO_2 _W powders show signals attributable to oxygenated species in proximity of V_O^+, V_{Zn}^-, $(V_{Zn}^-)_2^-$ and Zn_i centers, while no spectroscopic features have been detected for ZnO/SiO_2 _S.

Upon PhOH contact, the ESR spectrum of ZnO/SiO_2_S reveals the exclusive presence of a weak isotropic signal, whose *g*-value, linewidth and high stability match with the typical behavior of a $PhenO^\bullet$ EPFR. Instead, ZnO/SiO_2_W displays again intense spectral features associated to oxygenated species in proximity of V_O^+, V_{Zn}^- and $(V_{Zn}^-)_2^-$ centers, while only a very small contribution to the spectrum attributable to $PhenO^\bullet$ radical species can be discovered by signals simulation.

These results indicate that the intrinsic defectivity of ZnO NPs exerts an influence on the final yield of EPFR generation, with V_O^+ and V_{Zn}^- defects possibly involved in dissociative adsorption or oxidation processes at the oxide surface, thus hindering the formation and stabilization of EPFR in ZnO/SiO_2_W.

All of these suggestions, will help to critically re-examine and complement outstanding results already reported in the literature, offering a significant guidance to the future understanding on the EPFRs generation mechanism and stability in dependence to the defect chemistry of metal oxides.

Attaining this overarching goal is particularly difficult and can be faced only by a combined computational and experimental approach.

SUPPORTING INFORMATION

Details on the spectroscopic characterizations of ZnO/SiO_2 systems are reported. This material is available free of charge via the Internet at http://pubs.acs.org.

AUTHORS INFORMATION

Corresponding Authors

* massimiliano.darienzo@unimib.it

ACKNOWLEDGMENTS

M.D. gratefully acknowledge Marco Marni for his support in the ESR characterization. This work was partially realized in the frame of the project ‘‘Materials for Energy’’, financed by MIUR (Italian Ministry of University and Research) in the frame of “Fondo per il finanziamento dei dipartimenti universitari di eccellenza” - D.L. n.232, 11/12/2016.

REFERENCES

[1] Vejerano, E. P.; Rao, G.; Khachatryan, L.; Cormier, S.A.; Lomnicki, S. Environmentally Persistent Free Radicals: Insights on a New Class of Pollutants. *Environmental Science & Technology* **2018**, *52*, 2468-2481.

[2] Lomnicki, S.; Truong, H.; Vejerano, E.; Dellinger, B. Copper Oxide-Based Model of Persistent Free Radical Formation on Combustion-Derived Particulate Matter. *Environ. Sci. Technol.* **2008,** *42,* 4982–4988.

[3] Kiruri, L. W.; Khachatryan, L.; Dellinger, B.; Lomnicki, S. Effect of Copper Oxide Concentration on the Formation and Persistency of Environmentally Persistent Free Radicals (EPFRs) in Particulates. *Environ. Sci. Technol.* **2014**, *48*, 2212−2217.

[4] Kelley, M. A.; Hebert, V. Y.; Thibeaux, T. M.; Orchard, M.A.; Hasan, F.; Cormier, S. A.; Thevenot, P. T.; Lomnicki, S. M.; Varner, K. J.; Dellinger, B. Latimer, B. M.; Dugas, T. R.. Model Combustion-Generated Particulate Matter Containing Persistent Free Radicals Redox Cycle to Produce Reactive Oxygen Species. *Chem Res Toxicol*. **2013**, *26*, 1862–1871.

[5] Truong, H.; Lomnicki, S.; Dellinger, B. Potential for Misidentification of Environmentally Persistent Free Radicals as Molecular Pollutants in Particulate Matter. *Environ. Sci. Technol.* **2010,** *44,* 1933–1939.

[6] Khachatryan, L.; Vejerano, E.; Lomnicki, S.; Dellinger, B. Environmentally Persistent Free Radicals (EPFRs). 1. Generation of Reactive Oxygen Species in Aqueous Solutions. *Environ. Sci. Technol.* **2011**, *45*, 8559–8566.

[7] Khachatryan, L.; Dellinger, B. Environmentally Persistent Free Radicals (EPFRs)-2. Are Free Hydroxyl Radicals Generated in Aqueous Solutions? *Environ. Sci. Technol.* **2011**, *45*, 9232–9239.

[8] Weber, R. Relevance of PCDD/PCDF formation for the evaluation of POPs destruction technologies − Review on current status and assessment gaps. *Chemosphere* **2007**, *67*, S 109–117.

[9] Grandesso, E.; Ryan, S.; Gullett, B.; Touati, A.; Collina, E.; Lasagni, M.; Pitea, D. Kinetic modeling of polychlorinated dibenzo p dioxin and dibenzofuran formation based on carbon degradation reactions. *Environ. Sci. Technol.* **2008**, *42*, 7218-7224.

[10] Cosentino, U.; Pitea, D.; Moro, G. Computational modelling of de novo synthesis of Dibenzofuran: oxidative pathways of Pyrene and Benzodibenzofuran. *Theor. Chem. Acc*. **2012**, *131*, 1–12.

[11] Huang, H.; Buekens, A. De novo synthesis of polychlorinated Dibenzo-p-Dioxins and dibenzofurans. Proposal of a mechanistic scheme. *Sci. Total Environ.* **1996**, *193*, 121–141.

[12] Lenoir, D.; Wehrmeier, A.; Schramm, K.-W.; Kaune, A.; Zimmermann, R.; Taylor, P. H.; Sidhu, S. S. Thermal formation of polychlorinated dibenzo-p-dioxins and –furans: Investigation on relevant pathways. *Environ. Eng. Sci.* **1998**, *15*, 37–47.

[13] Dellinger, B.; Lomnicki, S.; Khachatryan, L.; Maskos, Z.; Hall, R. W.; Adounkpe, J.; McFerrin, C.; Truong, H. Formation and Stabilization of Persistent Free Radicals. *P. Combust. Inst.* **2007**, *31*, 521–528.

[14] Dellinger, B.; Pryor, W.A.; Cueto, R.; Squadrito, G.L.; Deutsch, W. A. Combustion-generated radicals and their role in the toxicity of fine particulate. *Organohalogen Compd*. **2000**, *46*, 302–305.

[15] Patterson, M. C.; Keilbart, N. D.; Kiruri, L. W.; Thibodeaux, C. A.; Lomnicki, S.; Kurtz, R. L.; Poliakoff, E. D.; Dellinger, B.; Sprunger, P. T. EPFR Formation from Phenol Adsorption on Al_2O_3 and TiO_2: EPR and EELS Studies. *J. Chem. Phys.* **2013**, *422*, 277–282.

[16] Vejerano, E.; Lomnicki, S.; Dellinger, B. Formation and Stabilization of Combustion-Generated Environmentally Persistent Free Radicals on an $Fe(III)_2O_3$/Silica Surface. *Environ. Sci. Technol.* **2011**, *45*, 589–594.

[17] Shah, A. S. V.; Langrish, J. P.; Nair, H.; McAllister, D. A.; Hunter, A. L.; Donaldson, K; Newby, D. E.; Mills, N. L. Global association of air pollution and heart failure: a systematic review and meta-analysis. *The Lancet* **2013**, *382*, 1039–1048.

[18] Atkinson, R. W.; Fuller, G. W.; Anderson, H. R.; Harrison, R. M.; Armstrong, B. Urban ambient particle metrics and health. A time series analysis. *Epidemiology* **2010**, *21*, 501–511.

[19] Thibodeaux, C. A. The electronic structure of environmentally persistent free radicals formed on metal oxide surfaces. PhD dissertation, McNeese State University, 2015.

[20] D'Arienzo, M.; Gamba, L.; Morazzoni, F.; Cosentino, U.; Greco, C.; Lasagni, M.; Pitea, D.; Moro, G.; Cepek, C.; Butera, V. Experimental and theoretical investigation on the catalytic generation of environmentally persistent free radicals from benzene. *J. Phys. Chem. C* **2017**, *121*, 9381−9393

[21] Vejerano, E.; Lomnicki, S.; Dellinger, B. Lifetime of Combustion-Generated Environmentally Persistent Free Radicals on Zn(II)O and Other Transition Metal Oxides. *J. Environ. Monit.* **2012**, *14*, 2803–2806.

[22] Thibodeaux, C. A.; Poliakoff, E. D.; Kizilkaya, O.; Patterson, M. C.; DiTusa, M. F.; Kurtz, R. L.; Sprunger, P. T. Probing environmentally significant surface radicals: Crystallographic and temperature dependent adsorption of phenol on ZnO. *Chem. Phys. Lett.* **2015**, *638*, 56–60.

[23] Patterson, M. C.; DiTusa, M. F.; McFerrin, C. A.; Kurtz, R. L.; Hall, R. W.; Poliakoff, E. D.; Sprunger, P. T. Formation of environmentally persistent free radicals (EPFRs) on ZnO at room temperature: Implications for the fundamental model of EPFR generation. *Chem. Phys. Lett.* **2018,** *670*, 5–10.

[24] Janotti, A; Van de Walle C.G. Fundamentals of zinc oxide as semiconductor. *Rep. Progr. Phys.* **2009**, *72*, 126501.

[25] Djuriić, A. B.; Ng, A. M. C.; Chen, X. Y. ZnO nanostructures for optoelectronics: Material properties and device applications. *Prog. Quantum Electron.* **2010**, *34*, 191–259;

[26] Willander, M.; Nur, O.; Sadaf, J. R.; Qadir, M. I.; Zaman, S.; Zainelabdin, A.; Bano, N.; Hussain, I. Luminescence from Zinc Oxide Nanostructures and Polymers and Their Hybrid Devices. *Materials* **2010**, *3*, 2643–2667.

[27] Schmidt-Mende, L.; MacManus-Driscoll, J. L. ZnO–nanostructures, defects, and devices. *Mater. Today* **2007**, *10*, 40–48.

[28] Hagemark, K. I. Defect structure of Zn-doped ZnO. *J. Solid State Chem.* **1976**, *16*, 293–299.

[29] Thomas, D. G. Interstitial zinc in zinc oxide. *J. Phys. Chem. Solids* **1957**, *3*, 229–237.

[30] Kurtz, M.; Strunk, J.; Hinrichsen, O.; Muhler, M.; Fink, K.; Meyer, B.; Wöll, C. Active Sites on Oxide Surfaces: ZnO-Catalyzed Synthesis of Methanol from CO and H_2. *Angew. Chem. Int. Ed.* **2005**, *44,* 2790– 2794.

[31] Ischenko, V.; Polarz, S.; Grote, D.; Stavarache, V.; Fink, K.; Driess, M. Zinc Oxide Nanoparticles with Defects, *Adv. Funct. Mater.* **2005**, *15,* 1945-1954;

[32] Polarz, S.; Strunk, J.; Ischenko, V.; Van den Berg, M. W. E.; Hinrichsen, O.; Muhler, M.; Driess, M. On the Role of Oxygen Defects in the Catalytic Performance of Zinc Oxide. *Angew. Chem. Int. Ed.* **2006**, *45*, 2965–2969.

[33] D'Arienzo, M.; Redaelli, M.; Di Credico, B.; Polizzi, S.; Scotti, R.; Morazzoni, F. New insights into the sensing mechanism of shape controlled ZnO particles. *RSC Adv.* **2016**, *6*, 52987-52997.

[34] Susanna, A.; Armelao, L.; Callone, E.; Dirè, S.; D'Arienzo, M.; Di Credico, B.; Giannini, L.; Hanel, T.; Morazzoni, F.; Scotti, R. ZnO nanoparticles anchored to silica filler. A curing accelerator for isoprene rubber composites. *Chemical Engineering Journal* **2015**, *275*, 245-252;

[35] Susanna, A.; D'Arienzo, M.; Di Credico, B.; Giannini, L.; Hanel, T.; Grandori, R.; Morazzoni, F.; Mostoni, S.; Santambrogio, C., Scotti, R. Catalytic effect of ZnO anchored silica nanoparticles on rubber vulcanization and cross-link formation. *European Polymer Journal* **2017**, *93*, 63-74.

[36] Scotti, R.; Conzatti, L.; D'Arienzo, M.; Di Credico, B.; Giannini, L.; Hanel, T.; Stagnaro, P.; Susanna, A.; Tadiello, L.; Morazzoni, F. Shape controlled spherical (0D) and rod-like (1D) silica nanoparticles in silica/styrene butadiene rubber nanocomposites: Role of the particle morphology on the filler reinforcing effect. *Polymer* **2014**, *55*, 1497-150;

[37] Tadiello, L.; D'Arienzo, M.; Di Credico, B.; Hanel, T.; Matejka, L.; Mauri, M.; Morazzoni, F.; Simonutti, R.; Spirkova, M.; Scotti, R. The filler–rubber interface in styrene butadiene

nanocomposites with anisotropic silica particles: morphology and dynamic properties. *Soft Matter* **2015**, *11*, 4022−4033.

[38] Adamski, A.; Spalek, T.; Sojka, Z. Application of EPR spectroscopy for elucidation of vanadium speciation in VO_x/ZrO_2 catalysts subject to redox treatment. *Res. Chem. Intermed*. **2003**, *29*, 793–804

[39] Ravikovitch, P.I.; Domhnaill, S.C.O.; Neimark, A.V.; Schuth, F.; Unger, K.K. Capillary hysteresis in nanopores: theoretical and experimental studies of nitrogen adsorption on MCM-41. *Langmuir* **1995**, *11*, 4765-4772;

[40] Lastoskie, C.; Gubbins, K. E.; Quirked, N. Pore Size Distribution Analysis of Microporous Carbons: A Density Functional Theory Approach. *J. Phys. Chem.* **1993**, *97*, 4786-4796.

[41] Moulder, J. F.; Stickle, W. F.; Sobol, P. E.; Bomben, K. D. in G. Chastain (Ed.), Handbook of X-ray Photoelectron Spectroscopy, Perkin Elmer Corporation, Eden Prairie (Minnesota), **1992**.

[42] Mahjoub, M. A. ; Monier, G. ; Robert-Goumet, C. ; Réveret, F. ; Echabaane, M. ; Chaudanson, D.; Petit, M.; Bideux, L. ; Gruzza, B. Synthesis and Study of Stable and Size-Controlled $ZnO–SiO_2$ Quantum Dots: Application as a Humidity Sensor. *J. Phys. Chem. C* **2016**, *120*, 11652−1662.

[43] Al-Gaashani, R.; Radiman, S. ; Daud, A. R. ; Tabet, N. ; Al-Douri, Y. XPS and optical studies of different morphologies of ZnO nanostructures prepared by microwave methods. *Ceramics International* **2013**, 39, 2283–2292.

[44] Özgür, Ü.; Alivov, Ya. I.; Liu, C.; Teke, A.; Reshchikov, M. A.; Dogan, S.; Avrutin, V.; Cho, S. J.; Morkov, H. A comprehensive review of ZnO materials and devices. *J. Appl. Phys.* **2005**, *98,* 1–103.

[45] Yi, L.; Xu, Z.; Hou, Y.; Zhang, X.; Wang, Y.; Xu, X. The ultraviolet and blue luminescence properties of ZnO:Zn thin film. *Chinese Sci. Bull.* **2001**, *46*, 1223–1226.

[46] Li, A. Pan, S.; Dou, X.; Zhu, Y.; Huang, X.; Yang, Y.; Li, G.; Zhang, L. Direct electrodeposition of ZnO nanotube arrays in anodic alumina membranes. *J. Phys. Chem. C* **2007**, *111*, 7288–7291.

[47] Camarda, P.; Messina, F.; Vaccaro, L.; Agnello, S.; Buscarino, G.; Schneider, R.; Popescu, R.; Gerthsen, D.; Lorenzi, R.; Gelardi, F. M.; Cannas, M. Luminescence mechanisms of defective ZnO nanoparticles. *Phys. Chem. Chem. Phys.* **2016**, *18*, 16237–16244.

[48] Drouilly, C.; Drouilly, C.; Krafft, J.-M.; Averseng, F.; Casale, S.; Bazer-Bachi, D.; Chizallet, C.; Lecocq, V.; Vezin, H.; Lauron-Pernot, H.; Costentin, G. ZnO oxygen vacancies formation and filling followed by in situ photoluminescence and in situ EPR. *J. Phys. Chem. C* **2012**, *116*, 21297–21307.

[49] Li, M.; Xing, G.; Xing, G.; Wu, B.; Wu, T.; Zhang, X.; Sum, T. C. Origin of green emission and charge trapping dynamics in ZnO nanowires. *Phys. Rev. B - Condens. Matter Mater. Phys.* **2013**, *87*, 115309.

[50] Xiong, G., Pal, U.; Serrano, J. G. Correlations among size, defects, and photoluminescence in ZnO nanoparticles. *J. Appl. Phys.* **2007**, *101*, 024317.

[51] Robin, I. C. Marotel, P.; El-Shaer, A. H.: Petukhov, V.; Bakin, A.; Waag, A.; Lafossas, M.; Garcia, J.; Rosina, M.; Ribeaud, A.; Brochen, S.; Ferret, P.; Feuillet, G. Compared optical properties of ZnO heteroepitaxial, homoepitaxial 2D layers and nanowires. *J. Cryst. Growth* **2009**, *311*, 2172–2175.

[52] Zhou, X. The origin of green emission of ZnO microcrystallites: Surface-dependent light emission studied by cathodoluminescence. *J. Phys. Chem. C* **2007**, *111*, 12091–12093.

[53] Lin, B.; Fu, Z.; Jia, Y. Green luminescent center in undoped zinc oxide films deposited on silicon substrates. *Appl. Phys. Lett.* **2001**, *79*, 943–945.

[54] Zeng, H.; Duaan, G.; Li, Y.; Yang, S.; Xu, X.; Cai, W. Blue luminescence of ZnO nanoparticles based on non-equilibrium processes: Defect origins and emission controls. *Adv. Funct. Mater.* **2010**, *20*, 561–572.

[55] Han, N. S.; Shi, H. S.; Seo, J. H.; Kim, S. Y.; Park, S. M.; Song, J. K. Defect states of ZnO nanoparticles: Discrimination by time-resolved photoluminescence spectroscopy. *J. Appl. Phys.* **2010**, *107*, 084306.

[56] Hu, J.; Pan, B. C. Electronic structures of defects in ZnO: Hybrid density functional studies. *J. Chem. Phys.* **2008**, *129*, 154706.

[57] Meyer, B. K.; Alves, H.; Hofmann, D. M.; Kriegseis, W.; Forster, D.; Bertram, F.; Christen, J.; Hoffmann, A.; Strassburg, M.; Dworzak, M.; Haboeck, U.; Rodina, A. V. Bound exciton and donor–acceptor pair recombinations in ZnO. *Phys. Status Solidi B* **2004**, *241*, 231–260.

[58] Evans, S. M.; Giles, N. C.; Halliburton, L. E.; Kappers, L. A. Further characterization of oxygen vacancies and zinc vacancies in electron-irradiated ZnO. J. Appl. Phys. **2008**, *103*, 043710.

[59] Polarz, S.; Roy, A.; Lehmann, M.; Driess, M.; Kruis, F. E.; Hoffmann, A.; Zimmer, P.; Structure–property–function relationships in nanoscale oxide sensors: a case study based on zinc oxide. *Adv. Funct. Mater.* **2007**, *17*, 1385–1391.

[60] Ischenko, V.; Polarz, S.; Grote, D.; Stavarache, V.; Fink, K.; Driess, M. Zinc oxide nanoparticles with defects, *Adv. Funct. Mater.* **2005**, *15*, 1945–1954.

[61] Jakes, P.; Erdem, E. Finite size effects in ZnO nanoparticles: An electron paramagnetic resonance (EPR) analysis. *Phys. Status Solidi RRL 5*, **2011**, *2*, 56–58.

[62] Kaftelen, H.; Ocakoglu, K.; Thomann, R.; Tu, S.; Weber, S.; Erdem, E. EPR and photoluminescence spectroscopy studies on the defect structure of ZnO nanocrystals. *Physical Review B* **2012**, ***86***, 014113.

[63] Parashar, S. K. S.; Murty, B. S.; Repp, S.; Weber, S.; Erdem, E. Investigation of intrinsic defects in core-shell structured ZnO nanocrystals. *Journal of Applied Physics* **2012**, *111*, 113712.

[64] Erdem, E. Microwave power, temperature, atmospheric and light dependence of intrinsic defects in ZnO nanoparticles: A study of electron paramagnetic resonance (EPR) spectroscopy. *Journal of Alloys and Compounds* **2014**, *605*, 34–44.

[65] Repp, S; Erdem, E. Controlling the exciton energy of zinc oxide (ZnO) quantum dots by changing the confinement conditions. *Spectrochimica Acta Part A: Molecular and Biomolecular Spectroscopy* **2016**, *152,* 637–644.

[66] Repp, S.; Weber, S.; Erdem, E. Defect evolution of nonstoichiometric ZnO quantum dots. *J. Phys. Chem. C* **2016**, *120*, 25124−25130.

[67] Kakazey, N. G.; Sreckovic, T. V.; Ristic, M. M. Electronic paramagnetic resonance investigation of the evolution of defects in zinc oxide during tribophysical activation. *J. Mat. Sci.* **1997**, *32*, 4619−4622.

[68] Maldonado, F.; Villamagua, L.; Rivera, R. DFT Analysis of the Adsorption of Phenol on the Nonpolar (1010) ZnO Surface. *J. Phys. Chem. C* **2019**, *123*, 12296−12304.

[69] Vannice, M. A. An analysis of the Mars–van Krevelen rate expression. *Catalysis Today* **2007**, *123*, 28−22.

[70] Skuja, L. Optically active oxygen-deficiency-related centers in amorphous silicon dioxide, *Journal of Non-Crystalline Solids* **1998**, *239*, 16−48.

[71] Sushko, P. V.; Mukhopadhyay, S.; Stoneham, A. M.; Shluger, A. L. Oxygen vacancies in amorphous silica: structure and distribution properties. *Microelectronic Engineering* **2005**, *80*, 292−295.

[72] Lenahan, P. M.; Conley, J. F. Jr. What can electron paramagnetic resonance tell us about the Si/SiO_2 system? *J. Vac. Sci. Technol. B* **1998**, *16,* 2134−2153.

[73] Saputera, W. H.; Tahini, H. A.; Sabsabi, M.; Tan, T. H.; Bedford, N. M.; Lovell, E.; Cui, Y.; Hart, J. N.; Friedmann, D.; Smith, S. C.; R. Amal; Scott, J. Light-induced synergistic multidefect sites on TiO_2/SiO_2 composites for catalytic dehydrogenation. ACS Catal. **2019**, *9*, 2674−2684.

TOC graphic

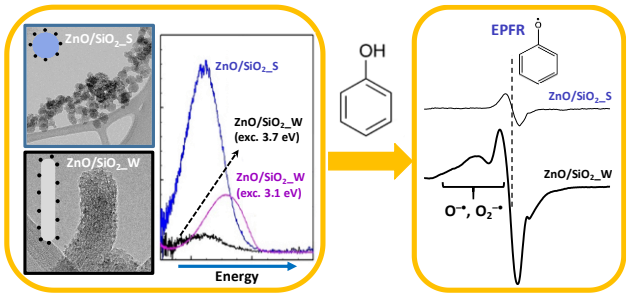
ZnO/SiO2_S
ZnO/SiO2_W
ZnO/SiO2_S
ZnO/SiO2_W
(exc. 3.7 eV)
ZnO/SiO2_W
(exc. 3.1 eV)
Energy
OH
EPFR
ZnO/SiO2_S
ZnO/SiO2_W
O•−, O2•−